Optics Letters

Incoherent lensless imaging via coherency back-propagation

Ahmed El-Halawany,[1,†] Andre Beckus,[2,†] H. Esat Kondakci,[1] Morgan Monroe,[1] Nafiseh Mohammadian,[1] George K. Atia,[2] and Ayman F. Abouraddy[1,*]

[1]CREOL, The College of Optics & Photonics, University of Central Florida, Orlando, Florida 32816, USA
[2]Department of Electrical and Computer Engineering, University of Central Florida, Orlando, Florida 32816, USA
*Corresponding author: raddy@creol.ucf.edu

Received 11 May 2017; accepted 30 June 2017; posted 10 July 2017 (Doc. ID 295169); published 8 August 2017

The two-point complex coherence function constitutes a complete representation for scalar quasi-monochromatic optical fields. Exploiting dynamically reconfigurable slits implemented with a digital micromirror device, we report on measurements of the complex two-point coherence function for partially coherent light scattering from a "scene" composing one or two objects at different transverse and axial positions with respect to the source. Although the intensity shows no discernible shadows in the absence of a lens, numerically back-propagating the measured complex coherence function allows estimating the objects' sizes and locations and, thus, the reconstruction of the scene subject to the effects of occlusion and shadowing.

OCIS codes: (030.1640) Coherence; (050.1940) Diffraction; (110.1650) Coherence imaging; (260.3160) Interference.

https://doi.org/10.1364/OL.42.003089

The complex field amplitude $E(\mathbf{r})$ associated with a coherent monochromatic scalar optical field provides a complete representation ($\mathbf{r}$ stands for the spatial coordinates) [1]. Once the amplitude and phase of $E(\mathbf{r})$ are measured by digital holography [2,3], acquiring the intensity in two planes [4–7], or wavefront sampling [8], for example, the field can be computed in any other plane using the diffraction propagator. When spatially incoherent light scatters off an object, the far-field intensity no longer retains distinctive features. Although the transfer function representing free propagation of incoherent light has no zeros [9], it nevertheless decays sharply with spatial frequency, thus significantly diminishing the contrast of far-field intensity variations and reducing the potential of identifying a scattering object. However, the two-point field correlations $G(\mathbf{r}_1, \mathbf{r}_2; \lambda)$ for pairs of points $\mathbf{r}_1$ and $\mathbf{r}_2$ in a quasi-monochromatic scalar field at a wavelength λ provide a complete representation [10]: determining $G(\mathbf{r}_1, \mathbf{r}_2; \lambda)$ at a plane allows evaluating it at any other plane. Measuring $G(\mathbf{r}_1, \mathbf{r}_2; \lambda)$ can be accomplished via wavefront sampling [11,12] or lateral-shear interferometry [13,14], among other possibilities [15–20]. Other approaches to incoherent lensless imaging include interferometric tomography [21] and rotational-shear interferometry [22].

In this Letter, we measure the coherence function of the optical field from an LED that is intercepted by a "scene" composing one or more obstacles. The partially coherent field evolves after the scene until intensity variations representative of the objects (shadows) are no longer discernible. The coherence function is measured by implementing dynamically reconfigurable double slits [23] using a digital micromirror device (DMD) [24]. For simplicity, we consider fields with one transverse coordinate x (assuming all fields are uniform along the other coordinate) and obtain the magnitude and phase of $G(x_1, x_2)$ at the detection plane from the visibility of the interferogram and the shift of the central fringe with respect to a fixed reference, respectively [11], and then back-propagate $G(x_1, x_2)$ towards the source to discover the scene and locate the scattering objects (we drop λ for convenience). We recently demonstrated that measuring G along the $x_2 = -x_1$ axis helps identify the transverse location and subtended angle (object width divided by its distance to the detection plane) of a single scattering object [25]. To identify the width and axial location separately, along with the transverse location and, furthermore, to reconstruct a more complex scene, a measurement of the full coherence function becomes necessary, as we proceed to demonstrate.

The field correlations between two points x_1 and x_2 in a plane at a distance z along the propagation axis can be described by a spatial coherence function $G(x_1, x_2; z) = \langle E(x_1)E^*(x_2)\rangle$, where $E(x)$ is a realization of a stochastic electric field and $\langle\cdot\rangle$ indicates an ensemble average, with the intensity lying along the diagonal $I(x_1; z) = G(x_1, x_1; z)$. Starting from a planar source having a coherence function $G(x', x''; z = 0)$, the coherence function at points x_1 and x_2 in a plane at $z = d$ after traversing a linear system having an impulse response function $h(x_1, x')$ is

$$G(x_1,x_2;d) = \iint \mathrm{d}x'\mathrm{d}x'' h(x_1,x')h^*(x_2,x'')G(x',x'';0). \quad (1)$$

Here, h needs not be unitary, so that systems including obstructions can be described in this way. In our experiments, h composes free-space propagation and interaction with opaque objects; see Fig. 1. Propagation a distance z is represented with a Fresnel integral of kernel $h_F(x_1, x'; z) \propto \exp\{i\frac{k}{2z}(x_1 - x')^2\}$ [1]. In one configuration, h composes a sequence of free propagation a distance d_1 from the source, a thin opaque object

represented by a transmittance $t(\tilde{x})$, followed by propagation a distance d_2 to the detection plane [Figs. 1(a) and 1(b)]. This cascade is represented by the impulse response function

$$h(x_1,x';d=d_1+d_2)=\int \mathrm{d}\tilde{x}\, h_{\mathrm{F}}(x_1,\tilde{x};d_2)\,t(\tilde{x})\,h_{\mathrm{F}}(\tilde{x},x';d_1), \quad (2)$$

and the coherence function at the detector is

$$G(x_1,x_2;d) = \iint \mathrm{d}\tilde{x}\mathrm{d}\tilde{\tilde{x}}\, h_{\mathrm{F}}(x_1,\tilde{x};d_2)\,h_{\mathrm{F}}^{*}(x_2,\tilde{\tilde{x}};d_2)\,t(\tilde{x})\,t^{*}(\tilde{\tilde{x}})\,G^{-}(\tilde{x},\tilde{\tilde{x}};d_1), \quad (3)$$

where $G^{-}(\tilde{x},\tilde{\tilde{x}};d_1)$ is the coherence function immediately before the object. We also define a coherence function immediately after the object $G^{+}(\tilde{x},\tilde{\tilde{x}};d_1)=t(\tilde{x})t^{*}(\tilde{\tilde{x}})G^{-}(\tilde{x},\tilde{\tilde{x}};d_1)$.

The specific form of the unitary operator for the Fresnel kernel $h_{\mathrm{F}}(x_1,x;z)$ [26] leads to the identity $h_{\mathrm{F}}^{*}(x,x_1;z)=h_{\mathrm{F}}(x,x_1;-z)$ and a composition rule $\int \mathrm{d}\tilde{x}\,h_{\mathrm{F}}(x_1,\tilde{x};d_2)h_{\mathrm{F}}(\tilde{x},x;d_1)=h_{\mathrm{F}}(x_1,x;d_1+d_2)$. By setting $h_{\mathrm{F}}(x_1,x;0)=\delta(x_1-x)$, $h_{\mathrm{F}}^{*}(x,x_1;z)$ becomes the inverse of $h_{\mathrm{F}}(x_1,x;z)$: $\int \mathrm{d}\tilde{x}\,h_{\mathrm{F}}(x_1,\tilde{x};z)h_{\mathrm{F}}^{*}(\tilde{x},x_1;z)=\delta(x_1-x)$. Therefore, starting from the coherence function at the detector plane given in Eq. (3), we can back-propagate G computationally a distance z towards the object by applying the operator $h_{\mathrm{F}}^{*}(x,x_1;z)=h_{\mathrm{F}}(x,x_1;-z)$. When $z=d_2$, the back-propagated coherence function becomes $G^{+}(\tilde{x},\tilde{\tilde{x}};d_1)$, and the intensity $I^{+}(\tilde{x};d_1)=|t(\tilde{x})|^2 I^{-}(\tilde{x};d_1)$, where $I^{-}(\tilde{x};d_1)$ is the intensity from the source immediately preceding the object.

Thus, our strategy is to measure the complex coherence function and then carry out the back-propagation to reconstruct the scene. For convenience, we utilize a rotated coordinate system (y_1,y_2) in lieu of (x_1,x_2), where $y_1=(x_1+x_2)/2$ and $y_2=(x_1-x_2)/2$, such that $G(x_1,x_2)\rightarrow G_{\mathrm{r}}(y_1,y_2)$. This basis rotation helps visualize G and facilitates computing its evolution along z by enabling a higher sampling efficiency in the (y_1,y_2)-plane compared to that in the (x_1,x_2)-plane. The intensity lies along the y_1-axis $I(y_1)=G_{\mathrm{r}}(y_1,0)$, whereas the coherence properties are best gleaned along the y_2-axis.

The coherence function $G_{\mathrm{r}}(y_1,y_2)$ is measured via dynamically reconfigurable double slits implemented by a DMD (Texas Instrument DLP 6500) that has 1024 × 768 pixels with a pixel pitch of 7.56 μm [Fig. 1(b)]. The width of each slit is ≈22.7 μm (three pixels). The separation between the slits $2y_2$ is varied in the range $0<2y_2<1500$ μm, whereas their center y_1 spans the range $-3<y_1<3$ mm with respect to the optical axis (DMD center) [25]. Following the DLP is a $4f$ imaging system (lenses L_1 and L_2 of focal lengths 10 and 20 cm, respectively, providing 2× magnification) and a $2f$ system composing a spherical lens L_3 of focal length 20 cm that produces interference patterns recorded by a charge-coupled device (The ImagingSource, DFK 31BU03), from which the magnitude and phase of G_{r} are extracted [25] [Fig. 1(b)]. The source is incoherent light from an LED (Thorlabs M625L3, peak wavelength of ≈633 nm and full width at half-maximum bandwidth ≈18 nm) filtered through a 1.3 nm bandwidth filter at a wavelength of 632.8 nm.

The experiment is initially carried out in the absence of objects (unobstructed propagation from the "primary" source to the detector) to calibrate the measurement system. The distance between the source and detector $d=1.44$ m is held fixed in all our experiments. We substitute the measured $G_{\mathrm{r}}(y_1,y_2;d)$ in the right-hand side of Eq. (1), replace $h(x_1,x)$ by $h_{\mathrm{F}}^{*}(x,x_1,-z)$, and set the back-propagation distance to $z=d$. A calibration phase is assessed that produces a maximum intensity profile at the source plane of the back-propagated signal.

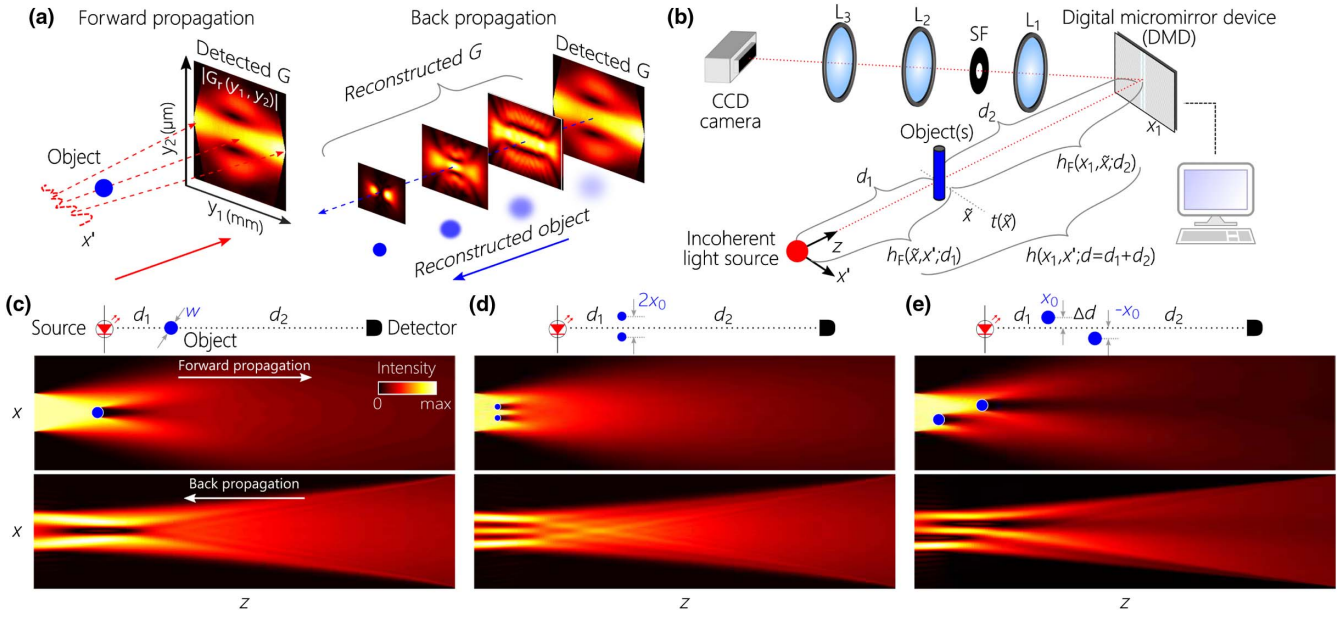

Fig. 1. (a) Concept of lensless coherence imaging. The coherence function $G(x_1,x_2;d)$ after scattering from an object is measured at a plane $z=d$, and then back-propagated computationally to the object. (b) Schematic of the measurement setup, where relay lenses ($\mathrm{L}_1=10$ cm and $\mathrm{L}_2=20$ cm) are followed by a third lens in a $2f$ configuration ($\mathrm{L}_3=20$ cm). SF: spatial filter. (c) A "scene" configuration composing a single on-axis object with diameters $w=0.5$ mm and $d_1=22$ cm. In the forward direction, the object casts a shadow that washes out in the far field. In the back-propagation direction, the object is replaced by an intensity dip that is symmetric with respect to the object location. (d) Configuration composing two identical objects located in the same axial plane with $w=0.25$ mm, $x_0=0.287$ mm, and $d_1=7$ cm. (e) Configuration composing two identical objects located in two different axial planes separated by a distance $\Delta d=15$ cm, with $w=0.5$ mm, $x_0=0.375$ mm, and $d_1=7$ cm. (c)–(e) In all simulations, $0\le z\le 144$ cm and the x-axis spans 6 mm.

We now proceed to reconstructing "secondary" sources—the scattering objects.

We first consider the case where an object (a metal wire of diameter $w = 0.5$ mm at $d_1 = 22$ cm from the source) obstructs the field [Fig. 1(c)]. Diffraction after the object smears out the shadow, as predicted by a forward-model calculation [Fig. 1(c)] and confirmed in the measured $|G_r(y_1, 0; d)|$ [Fig. 2(a)]. By back-propagating the measured complex $G_r(y_1, y_2; d)$ [Figs. 2(a) and 2(b)] and increasing the back-propagation distance z, we construct the coherence function $G_r(y_1, y_2; z)$ at planes preceding the detection plane axially and gradually approaching the object, samples of which are shown in Fig. 2(d). From $G_r(y_1, y_2; z)$, we can extract the evolution of the intensity distribution $I(y_1; z)$ along the propagation axis by setting $y_2 = 0$ [Fig. 2(d)]. Note the different scales along transverse (vertical) direction x (4 mm) and longitudinal (horizontal) direction z (1.44 m) in Fig. 2(c).

The back-propagation yields a localized "shadow" of the object in the intensity profile that provides an estimate of the size and position (transverse and longitudinal) of the object [Fig. 2(c)]. For simplicity, we consider the "focal plane" to be the plane in which the dip in the intensity profile reaches its minimum. The error in estimating the location of the object from the detection plane is ≈7.4%. Note that the width of the intensity distribution decreases as we travel backward, and at the object plane is quite narrow, contrary to the extremely wide field produced from the LED. This is due to the finite size of the detection area: the source field far from the optical axis at the object plane does not contribute to the detection plane.

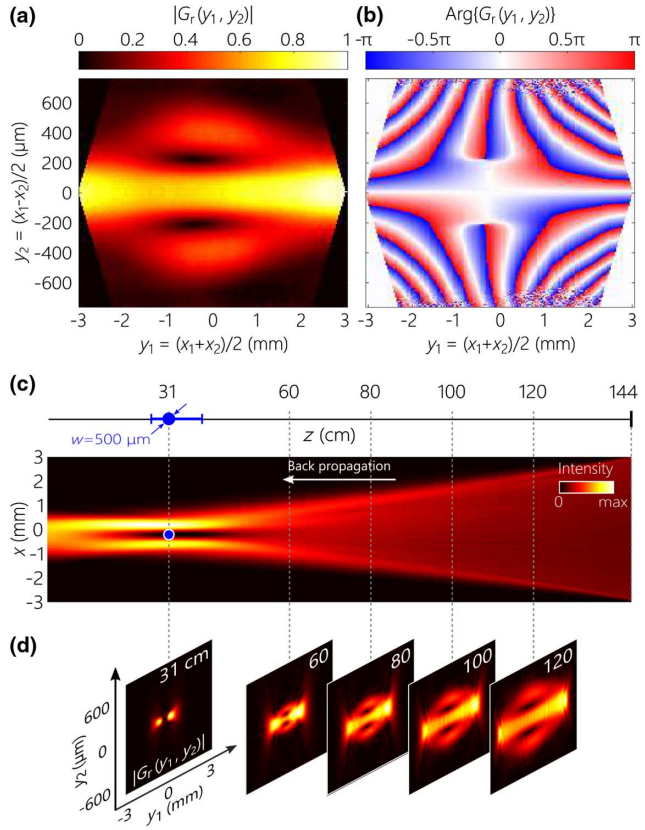

Fig. 2. Back-propagation of the measured coherence function for the configuration in Fig. 1(c) composing a single object. (a) Measured amplitude $|G_r(y_1, y_2)|$ and (b) wrapped phase $\text{Arg}\{G_r(y_1, y_2)\}$ of the coherence function in the rotated coordinate system (y_1, y_2). The phase-wrapping has no effect on the back-propagation. (c) Back-propagated intensity $I(x; z)$ along z. The estimated object width is 380 μm by finding the halfway point between the dip minimum and peak magnitude of the intensity in the object plane. The axial error bar indicates where the magnitude remains within 5% of the minimum. (d) Back-propagated $G_r(y_1, y_2; z)$ at selected distances from the source.

We next consider a scenario where two co-planar objects, two metal wires of equal diameters $w = 0.25$ mm, are separated by $2x_0 = 0.575$ mm and placed at a distance $d_1 = 7$ cm from the source [Fig. 3(a)]. The shadow cast by the two objects has mostly smeared out at the detector plane; see $|G_r(y_1, 0; d)|$ in Fig. 3(a). The measured complex $G_r(y_1, y_2; d)$ [Figs. 3(a) and 3(b)] is back-propagated [Fig. 3(d)], and we extract the evolution of the intensity $I(y_1; z)$ along the propagation axis as before [Fig. 3(c)]. The back-propagation yields two localized "shadows" of the objects in the intensity profile from which we estimate the size and position of the two objects [Fig. 3(c)]. The error in estimating the location of the objects from the detection plane is ≈3.6%.

Finally, we consider a scenario where two objects (metal wires of diameter $w = 0.5$ mm each) are located in different planes along the propagation axis. The first object is at a distance $d_1 = 7$ cm from the source and is displaced to a position $x_0 = 0.375$ mm from the optical axis, and the second object follows it at a further distance Δd along z and is displaced to a symmetrically opposite transverse position $-x_0$ [Fig. 1(e)].

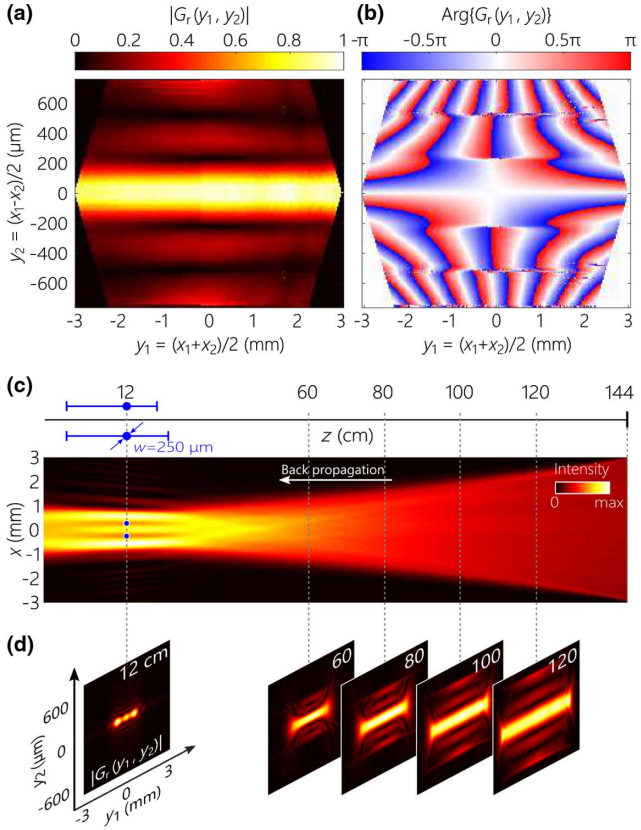

Fig. 3. Same as in Fig. 2, except that the two-object scene in Fig. 1(d) is employed. The two identical objects have a diameter of 250 μm (smaller than that of the object in Fig. 2) and are placed in the same transverse plane. The object widths are estimated at ≈280 μm at $d_1 = 12$ cm located at $x_0 \approx -284$ and ≈253 μm.

Whereas the shadow cast by the first object (closest to the source) has mostly washed out, there is a remnant shadow from the second object (closest to the detection plane); see $|G_r(y_1, 0; d)|$ in Fig. 4(a). The measured complex $G_r(y_1, y_2; d)$ [Figs. 4(a) and 4(b)] is back-propagated [Fig. 4(d)], and we extract the evolution of the intensity $I(y_1; z)$ along the propagation axis as before [Fig. 4(c)]. Over the course of the back-propagation, two localized "shadows" emerge. First, a shadow of the object closest to the detection plane emerges at $d_1 = 40$ cm in the intensity profile. We do not observe a shadow of the second object at this plane. By continuing the back-propagation procedure, the first observed shadow starts to smear out, while a second shadow associated with the object closest to the source emerges. From these calculations, we can estimate the size and locations of the two objects [Fig. 4(c)]. The errors in estimating the location of the objects from the detection plane are ≈14.8% and ≈ −3.6%.

We now discuss some of the limitations of this approach. The back-propagation is exact only if the detector is of infinite size. The finite detector size leads to imperfections in reconstructing the scene, e.g., a finite resolution for distinguishing objects located at neighboring transverse or longitudinal positions. The results in Fig. 2 identify a limitation of this approach, namely that the region immediately behind the object (which is occluded from the perspective of the detector) represents a "null space" for the procedure: a small object placed in the immediate vicinity behind the object will be difficult to observe. In general, when an object obstructs the light path, some information from the preceding planes is lost. For example, if two objects are placed in two different planes, the object closer to the detector will occlude the farther object. Increasing the size of the detection plane helps alleviate these limitations. Finally, strictly speaking, the back-propagation procedure described above does not necessitate knowledge of the source for a successful reconstruction of the scene. We carried out a reference measurement for calibration only. An accurate measurement of $G_r(y_1, y_2)$ suffices for the back-propagation procedure.

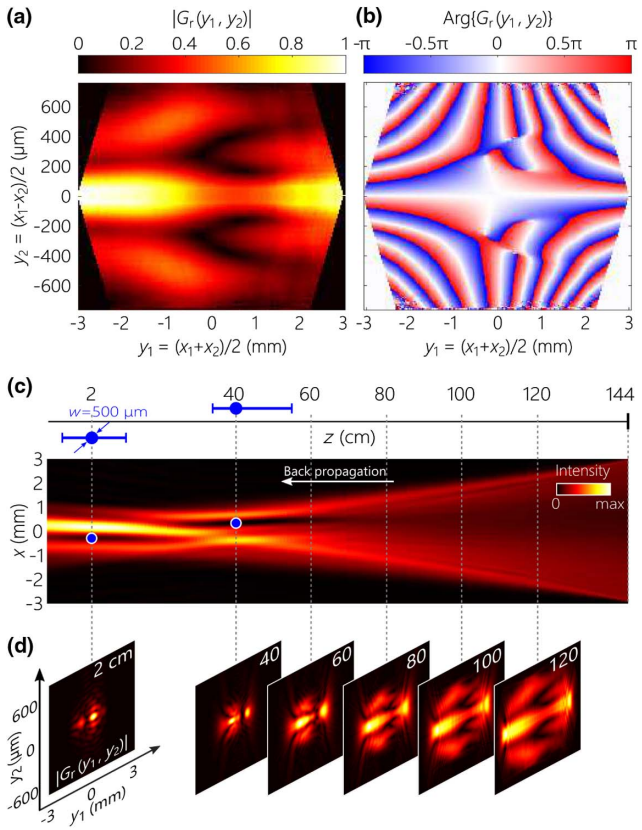

Fig. 4. Same as in Fig. 2, except that the two-object scene in Fig. 1(e) is employed. The two identical objects have a diameter of 500 μm and are placed off the central axis in different axial planes. The object widths are estimated at ≈400 μm, $x_0 \approx -321$ μm, for the object closest to the source and $x_0 \approx 309$ μm for the other object.

In conclusion, we have demonstrated that back-propagating the two-point complex coherence function measured in a plane can be utilized to reconstruct a scene containing scattering objects with no need for a lens. The coherence function needs to be measured at only one plane, even when the intensity lacks spatial variations. Acquiring the complex coherence function is made practical by utilizing a DMD that implements dynamically reconfigurable double slits.

Funding. Defense Advanced Research Projects Agency (DARPA), Defense Science Office (DSO) (HR0011-16-C-0029).

†These authors contributed equally to this Letter.

REFERENCES

1. B. E. Saleh and M. C. Teich, *Fundamentals of Photonics*, 2nd ed. (Wiley-Interscience, 2007).
2. I. Yamaguchi and T. Zhang, Opt. Lett. **22**, 1268 (1997).
3. M. K. Kim, *Digital Holographic Microscopy* (Springer, 2011).
4. R. W. Gerchberg and W. O. Saxton, Optik **35**, 237 (1972).
5. J. R. Fienup, Appl. Opt. **21**, 2758 (1982).
6. A. F. Abouraddy, O. Shapira, M. Bayindir, J. Arnold, F. Sorin, D. S. Hinczewski, J. D. Joannopoulos, and Y. Fink, Nat. Mater. **5**, 532 (2006).
7. S. Witte, V. T. Tenner, D. W. E. Noom, and K. S. E. Eikema, Light Sci. Appl. **3**, e163 (2014).
8. G. Vdovin, H. Gong, O. Soloviev, P. Pozzi, and M. Verhaegen, J. Opt. **17**, 122001 (2015).
9. N. George, Opt. Commun. **133**, 22 (1997).
10. L. Mandel and E. Wolf, *Optical Coherence and Quantum Optics* (Cambridge University, 1995).
11. B. J. Thompson and E. Wolf, J. Opt. Soc. Am. **47**, 895 (1957).
12. M. Françon and S. Mallick, in *Progress in Optics*, E. Wolf, ed. (North-Holland, 1967), Vol. **VI**, pp. 73–104.
13. C. Iaconis and I. A. Walmsley, Opt. Lett. **21**, 1783 (1996).
14. C.-C. Cheng, M. G. Raymer, and H. Heier, J. Mod. Opt. **47**, 1237 (2000).
15. M. Santarsiero and R. Borghi, Opt. Lett. **31**, 861 (2006).
16. A. I. Gonzáles and Y. Mejía, J. Opt. Soc. Am. A **28**, 1107 (2011).
17. S. Divitt and L. Novotny, Optica **2**, 95 (2015).
18. B. Stoklasa, L. Motka, J. Rehacek, Z. Hradil, and L. L. Sáchez-Soto, Nat. Commun. **5**, 3275 (2014).
19. K. H. Kagalwala, H. E. Kondakci, A. F. Abouraddy, and B. E. A. Saleh, Sci. Rep. **5**, 15333 (2015).
20. K. A. Sharma, T. G. Brown, and M. A. Alonso, Opt. Express **24**, 16099 (2016).
21. D. L. Marks, R. A. Stack, D. J. Brady, D. C. Munson, Jr., and R. B. Brady, Science **284**, 2164 (1999).
22. D. L. Marks, R. A. Stack, and D. J. Brady, Appl. Opt. **38**, 1332 (1999).
23. H. Partanen, J. Turunen, and J. Tervo, Opt. Lett. **39**, 1034 (2014).
24. D. Dudley, W. M. Duncan, and J. Slaughter, Proc. SPIE **4985**, 14 (2003).
25. H. E. Kondakci, A. Beckus, A. El Halawany, N. Mohammadian, G. K. Atia, and A. F. Abouraddy, Opt. Express **25**, 13087 (2017).
26. A. Stern, AIP Conf. Proc. **860**, 225 (2006).